J. Fluid Mech. (1999), *vol.* 398, *pp.* 271–297. Printed in the United Kingdom

© 1999 Cambridge University Press

Gravito-inertial waves in a rotating stratified sphere or spherical shell

By B. DINTRANS[1], M. RIEUTORD[1,2] AND L. VALDETTARO[3]

[1] Observatoire Midi-Pyrénées, 14 av. E. Belin, F-31400 Toulouse, France

[2] CERFACS, 42, Avenue Coriolis, F-31057 Toulouse, France

[3] Dipartimenta di Matematica, Politecnico di Milano, Piazza L. da Vinci, 32, 20133 Milano, Italy

(Received 28 April 1998 and in revised form 9 June 1999)

The properties of gravito-inertial waves propagating in a stably stratified rotating spherical shell or sphere are investigated using the Boussinesq approximation. In the perfect fluid limit, these modes obey a second-order partial differential equation of mixed type. Characteristics propagating in the hyperbolic domain are shown to follow three kinds of orbits: quasi-periodic orbits which cover the whole hyperbolic domain; periodic orbits which are strongly attractive; and finally, orbits ending in a wedge formed by one of the boundaries and a turning surface. To these three types of orbits, our calculations show that there correspond three kinds of modes and give support to the following conclusions. First, with quasi-periodic orbits are associated regular modes which exist at the zero-diffusion limit as smooth square-integrable velocity fields associated with a discrete set of eigenvalues, probably dense in some subintervals of $[0, N]$, N being the Brunt–Väisälä frequency. Second, with periodic orbits are associated singular modes which feature a shear layer following the periodic orbit; as the zero-diffusion limit is taken, the eigenfunction becomes singular on a line tracing the periodic orbit and is no longer square-integrable; as a consequence the point spectrum is empty in some subintervals of $[0, N]$. It is also shown that these internal shear layers contain the two scales $E^{1/3}$ and $E^{1/4}$ as pure inertial modes (E is the Ekman number). Finally, modes associated with characteristics trapped by a wedge also disappear at the zero-diffusion limit; eigenfunctions are not square-integrable and the corresponding point spectrum is also empty.

1. Introduction

Gravito-inertial waves are waves that propagate in a rotating stably stratified fluid. When studying the dynamics of stars, such waves are important as they are good candidates for transporting angular momentum and chemical elements in stably stratified regions such as radiative zones (see Kumar & Quateart 1997 and Zahn, Talon & Matias 1997). Still in the astrophysical context, the variability of certain rapidly rotating stars such as γ Doradus (Balona *et al.* 1996) cannot be understood with perturbative analysis of pure gravity modes as commonly done on slowly rotating stars (see Unno *et al.* 1979); a possible explanation is that such pulsations result from the excitation of gravito-inertial modes. In the geophysical context, such waves are also of interest, especially in oceans where they should play an important part in mixing processes (Maas *et al.* 1997).

The properties of the oscillations of a rotating stratified fluid in a container have been investigated by Friedlander & Siegmann (1982*a*). Stewartson & Walton (1976) attacked this problem in the limiting case of a thin shell. They found that the existence of singular solutions is connected with the strength of the stratification, a result which we confirm for the general case. Friedlander & Siegmann (1982*a*, *b*) and Friedlander (1982) were the first to report on the general properties of such modes, showing in particular the mixed nature of the partial differential equations governing the perfect fluid oscillations. They demonstrated that when the Brunt–Väisälä frequency is proportional to the radial distance, the turning surface separating the hyperbolic domain from the elliptic one is either a hyperboloid or an ellipsoid. Then, the asymptotic case of weak stratification was investigated more thoroughly by Friedlander (1987).

The aim of the present paper is to further investigate the properties of gravito-inertial modes and, we hope, give a better understanding of their complicated dynamics. It extends our work on pure inertial waves in a spherical shell, hereafter referred to as paper I (Rieutord & Valdettaro 1997). (Appendix D of the present paper is an addendum to paper I.) As in that paper, we restrict ourselves to axisymmetric modes, but we shall see that our conclusions are general.

Pure mathematical approaches are difficult because linearized Euler equations are degenerate elliptic and no general spectral theorem applies (S. Friedlander, private communication); in addition, the problem's variables are not separable, rendering the analysis intractable; we thus turn towards numerical solutions of modal equations that include viscosity and thermal diffusivity. Thanks to a powerful eigenvalue solver, we have been able to explore a wide range of viscosities and diffusivities and therefore to give a good picture of gravito-inertial modes in the limit of a perfect fluid. We recall that astrophysical or geophysical situations always require very small diffusivities.

Our results may be summarized as follows: as the perfect fluid limit is approached, most of the modes become singular and only a countable set of regular modes may survive in some region of the spectrum. We use the term regular modes to mean solutions of the inviscid equations with at least a continuous square-integrable velocity field. Singular solutions are all other types of velocity fields which do not meet the above requirements. In fact, singular modes are modes whose characteristics are focused towards an attractor: a wedge (formed by turning surfaces and boundaries) or a periodic orbit; their velocity field is not square-integrable; they usually also contain a singularity on the axis and possibly one at the critical latitude, but these two singularities are square-integrable. Our results give strong evidence that the regular or singular nature of modes can be determined from purely geometric considerations based on the paths of characteristics.

This classification of modes has far-reaching consequences for the dynamics of stars: regular modes are the best candidates for driving pulsations of variable stars since they are the least damped, while singular modes will be efficient at transporting angular momentum or, more generally, at mixing. Such modes may be excited by various effects such as the kappa-mechanism, tidal forcing or turbulent plumes of a neighbouring convection zone.

The ratio of the inner radius to the outer radius of the shell, η, is set in most cases to 0.35. This is the geometry of the radiative zone of a three-solar-mass star as well as the geometry of the liquid core of the Earth, although this latter application, which is considered in Rieutord (1999), is not to be taken literally since this body may be stably stratified only in a small fraction of its volume (Lister & Buffett 1995; Rieutord 1995).

The plan of the paper is the following: After setting out the equations of the system and recalling the method we use for solving them (§ 2), we first investigate the different ways characteristics behave (§ 3.1) as a function of frequency and stratification. After a classification of the different behaviours, we inspect the corresponding numerical solutions of the partial differential equations and show how the propagation of characteristics influences the shape of the modes (§ 3.2). The evolution of mode patterns as viscosity or thermal diffusion are decreased is also considered (§ 3.3). We lastly present a study of the distribution of eigenvalues in the complex plane (§ 3.4). We conclude with a general discussion on inertial and gravito-inertial modes as well as on the immediate implications for astrophysics.

2. Formulation

2.1. *The equations using the Boussinesq approximation.*

For the sake of simplicity, we consider a spherical shell where heat sinks are uniformly distributed so that the temperature gradient is of the form $\beta \boldsymbol{r}/R$, β being a positive constant and R the outer radius of the shell. Using the Boussinesq approximation, we are led to consider a gravity field of the form $\boldsymbol{g} = -g_0 \boldsymbol{r}/R$, g_0 being the acceleration due to gravity at $r = R$. Such a configuration has been employed several times in the past for studies of convection (with heat sinks replaced by heat sources) in spherical geometry (see Chandrasekhar 1961 or more recently Zhang 1995). In order to easily connect the present results with those of paper I, we use the same length and time scales. These are the radius of the outer shell R for the length scale and $(2\Omega)^{-1}$ for the time scale, Ω being the angular velocity ($\boldsymbol{\Omega} = \Omega \boldsymbol{e}_z$). Equations of perturbations in a rotating frame are well known and we directly write their non-dimensional linearized form:

$$\left.\begin{aligned} &\lambda \boldsymbol{u} + \boldsymbol{e}_z \wedge \boldsymbol{u} = -\nabla \Pi + N^2 \Theta \boldsymbol{r} + E \Delta \boldsymbol{u}, \\ &\nabla \cdot \boldsymbol{u} = 0, \\ &\lambda \Theta + r u_r = (E/\mathscr{P}) \Delta \Theta, \end{aligned}\right\} \tag{2.1}$$

where we assumed a time-dependence of the form $\exp(\lambda t)$; we will often write the complex eigenvalue $\lambda = \tau + \mathrm{i}\omega$, τ being the damping rate and ω the frequency. The variables $\boldsymbol{u}$, Π and Θ are respectively the velocity, reduced pressure and temperature perturbations. E denotes the Ekman number, $\mathscr{P}$ the Prandtl number and N the dimensionless Brunt–Väisälä frequency with

$$E = \frac{\nu}{2\Omega R^2}, \qquad \mathscr{P} = \frac{\nu}{\kappa}, \qquad N^2 = \frac{\alpha \beta g_0}{4\Omega^2}, \tag{2.2}$$

where ν is the kinematic viscosity, κ is the thermal diffusivity, α is the coefficient of volume expansion and β is the temperature gradient at $r = 1$. The fluid's stratification is stable; therefore, $N^2 > 0$.

As in paper I, we use stress-free boundary conditions for the velocity. Such conditions are more realistic for applications to stars or planets; they prove also to be more convenient for showing internal shear layers of the solutions; in fact, as shown by Fotheringham & Hollerbach (1998) on the case of inertial modes, solutions are only mildly sensitive to boundary conditions. Thus on both shells:

$$\boldsymbol{u} \cdot \boldsymbol{e}_r = \boldsymbol{0} \quad \text{and} \quad \boldsymbol{e}_r \times ([\boldsymbol{\sigma}] \boldsymbol{e}_r) = \boldsymbol{0} \tag{2.3}$$

with $[\boldsymbol{\sigma}]$ being the stress tensor and $\boldsymbol{e}_r$ the unit radial vector. Concerning the boundary

conditions on temperature, we assumed for simplicity a perfect conductor on both shells. Thus $\Theta = 0$ on the inner and outer shells, although the use of insulating boundary conditions introduces only minor differences from solutions presented below as no thermal boundary layer exists.

2.2. *Numerics*

Following Rieutord (1987, 1991), we expand the velocity and temperature on spherical harmonics as

$$\boldsymbol{u} = \sum_{\ell=0}^{+\infty} \sum_{m=-\ell}^{+\ell} u_m^\ell(r)\boldsymbol{R}_\ell^m + v_m^\ell(r)\boldsymbol{S}_\ell^m + w_m^\ell(r)\boldsymbol{T}_\ell^m, \quad \Theta = \sum_{\ell=0}^{+\infty} \sum_{m=-\ell}^{+\ell} t_m^\ell(r) Y_\ell^m(\theta,\phi), \tag{2.4}$$

where $Y_\ell^m(\theta,\phi)$ denotes the normalized spherical harmonics and

$$\boldsymbol{R}_\ell^m = Y_\ell^m(\theta,\phi)\boldsymbol{e}_r, \qquad \boldsymbol{S}_\ell^m = \nabla Y_\ell^m, \qquad \boldsymbol{T}_\ell^m = \nabla \times \boldsymbol{R}_\ell^m.$$

Taking the curl of the momentum equation and projecting onto the vectorial harmonics $\boldsymbol{R}_\ell^m$ and $\boldsymbol{T}_\ell^m$, we obtain the radial equations satisfied by $u_m^\ell(r)$, $w_m^\ell(r)$ and $t_m^\ell(r)$:

$$\left.\begin{aligned}
&E\Delta_\ell w_m^\ell + \left[\frac{\mathrm{i}m}{\ell(\ell+1)} - \lambda\right] w_m^\ell \\
&\quad = -A(\ell,m) r^{\ell-1} \frac{\mathrm{d}}{\mathrm{d}r}\left(\frac{u_m^{\ell-1}}{r^{\ell-2}}\right) - A(\ell+1,m) r^{-\ell-2} \frac{\mathrm{d}}{\mathrm{d}r}\left(r^{\ell+3} u_m^{\ell+1}\right), \\
&E\Delta_\ell \Delta_\ell (r u_m^\ell) + \left[\frac{\mathrm{i}m}{\ell(\ell+1)} - \lambda\right] \Delta_\ell (r u_m^\ell) \\
&\quad = B(\ell,m) r^{\ell-1} \frac{\mathrm{d}}{\mathrm{d}r}\left(\frac{w_m^{\ell-1}}{r^{\ell-1}}\right) + B(\ell+1,m) r^{-\ell-2} \frac{\mathrm{d}}{\mathrm{d}r}\left(r^{\ell+2} w_m^{\ell+1}\right) + N^2 \ell(\ell+1) t_m^\ell, \\
&(E/\mathscr{P})\Delta_\ell t_m^\ell - \lambda t_m^\ell = r u_m^\ell,
\end{aligned}\right\} \tag{2.5}$$

where

$$A(\ell,m) = \frac{1}{\ell^2}\sqrt{\frac{\ell^2-m^2}{4\ell^2-1}}, \quad B(\ell,m) = \ell^2(\ell^2-1)A(\ell,m), \quad \Delta_\ell = \frac{1}{r}\frac{\mathrm{d}^2}{\mathrm{d}r^2} r - \frac{\ell(\ell+1)}{r^2}.$$

The boundary conditions for radial functions are now

$$\left.\begin{aligned}
u_m^\ell &= \frac{\partial^2 r u_m^\ell}{\partial r^2} = \frac{\partial}{\partial r}\left(\frac{w_m^\ell}{r}\right) = 0, \\
t_m^\ell &= 0.
\end{aligned}\right\} \tag{2.6}$$

Formally, the system (2.5) may be written as

$$\mathscr{M}_A \boldsymbol{\psi}_m = \lambda \mathscr{M}_B \boldsymbol{\psi}_m, \tag{2.7}$$

where $\mathscr{M}_A$ and $\mathscr{M}_B$ are two differential operators and λ is the complex eigenvalue

associated with eigenvector $\boldsymbol{\psi}_m$:

$$\boldsymbol{\psi}_{m^+} \left| \begin{array}{l} u_m^m(r) \\ t_m^m(r) \\ w_m^{m+1}(r) \\ u_m^{m+2}(r) \\ t_m^{m+2}(r) \\ \vdots \\ \vdots \end{array} \right. , \quad \text{or} \quad \boldsymbol{\psi}_{m^-} \left| \begin{array}{l} w_m^m(r) \\ u_m^{m+1}(r) \\ t_m^{m+1}(r) \\ w_m^{m+2}(r) \\ u_m^{m+3}(r) \\ \vdots \\ \vdots \end{array} \right. .$$

Here $\boldsymbol{\psi}_{m^+}$ and $\boldsymbol{\psi}_{m^-}$ denote respectively symmetric or antisymmetric solutions with respect to the equator. The differential eigenvalue problem (2.7) is discretized in the radial direction using the values of the $\boldsymbol{\psi}_m$ on the Gauss–Lobatto grid associated with Chebyshev polynomials. After truncating at order L for the spherical harmonics basis and at order N_r for the Chebyshev basis, the problem becomes a generalized algebraic eigenvalue problem whose dimension is of order $L \times N_r$. Two algorithms will then be used:

(*a*) the QZ algorithm for computing the whole spectrum of complex eigenvalues λ and the associated eigenvectors $\boldsymbol{\psi}_m$;

(*b*) the incomplete Arnoldi–Chebyshev algorithm for computing some pairs $(\lambda, \boldsymbol{\psi}_m)$ around a given value of λ (Arnoldi 1951; Saad 1992).

All the results of these computations (§ 3.2 and following) have been obtained for $m = 0$ modes.

3. Results

3.1. *Turning surfaces and paths of characteristics*

3.1.1. *Turning surfaces and mode classification*

In the case of pure inertial modes, the inviscid pressure equation (i.e. the Poincaré equation) is hyperbolic in the whole domain. The characteristics associated with this hyperbolic problem form a web of straight lines which reflect from the boundaries and propagate in the whole shell (see paper I). Adding a stratification deeply modifies this structure by making the pressure operator of mixed type with elliptic and hyperbolic regions separated by a turning surface. The equation of this surface was first derived by Friedlander & Siegmann (1982*b*). It reads

$$\frac{s^2}{\omega^2 - 1} + \frac{z^2}{\omega^2} = \frac{1}{N^2}, \tag{3.1}$$

where (s, z) are cylindrical coordinates. According to the values of (ω, N), this surface is either a hyperboloid or an ellipsoid. Following Friedlander & Siegmann, we distinguish four types of modes:

two 'hyperbolic modes', hereafter called H-modes, with hyperboloidal turning surfaces:

$$\left. \begin{array}{ll} H_1: & N < \omega < 1, \\ H_2: & 0 < \omega < \min(1, N), \end{array} \right\} \tag{3.2}$$

for which the turning surface is respectively outside or inside the shell.

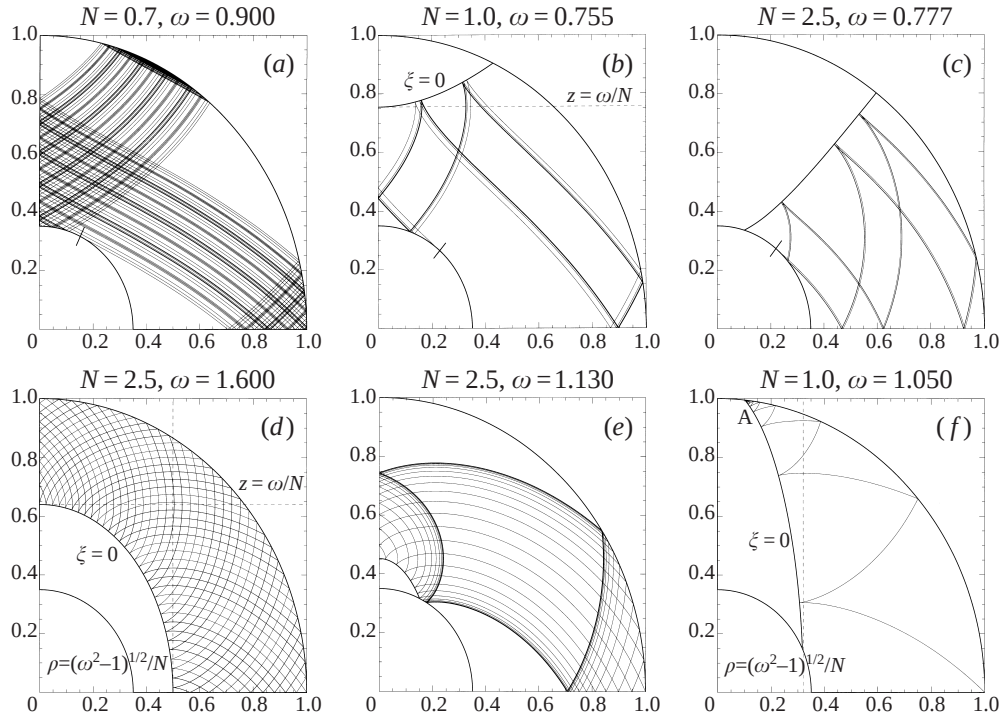

FIGURE 1. Paths of characteristics for H_1-modes (a), H_2-modes (b, c), E_1-modes (d, e), and E_2-modes (f). The tick on the inner shell marks the critical latitude $\sin\vartheta_c = \omega$. The apex of the turning surface $\xi = 0$ is on the axis at $z_c = \omega/N$. The semi-minor axis for E-modes is at $s = \sqrt{\omega^2 - 1}/N$. A hundred reflections have been drawn on each diagram.

two 'elliptic modes', hereafter called E-modes, with ellipsoidal turning surfaces:

$$\left.\begin{aligned} E_1 :&\quad 1 < \omega < N, \\ E_2 :&\quad \max(1, N) < \omega < \sqrt{1 + N^2}, \end{aligned}\right\} \tag{3.3}$$

for which the hyperbolic region respectively does and does not encompass the rotation axis.

These four types of modes are illustrated in figure 1 for a shell with $\eta = 0.35$. The curved characteristics now reflect both from the boundaries and from turning surfaces; they are solutions of the following differential equation (Friedlander & Siegmann 1982*b*):

$$\frac{\mathrm{d}z}{\mathrm{d}s} = \frac{zsN^2 \pm \xi^{1/2}}{\omega^2 - N^2 z^2}, \qquad \xi = \omega^2 N^2 s^2 + (1 - \omega^2)(\omega^2 - N^2 z^2). \tag{3.4}$$

We note that the turning surface (3.1) corresponds to $\xi = 0$ and that characteristics are normal to it.

Non-axisymmetric modes share the same characteristics and turning surfaces as axisymmetric ones, since the inclusion of an $\exp(\mathrm{i}m\phi)$-dependence does not modify the second-order derivative terms. The following results on characteristics' paths are therefore independent of this symmetry.

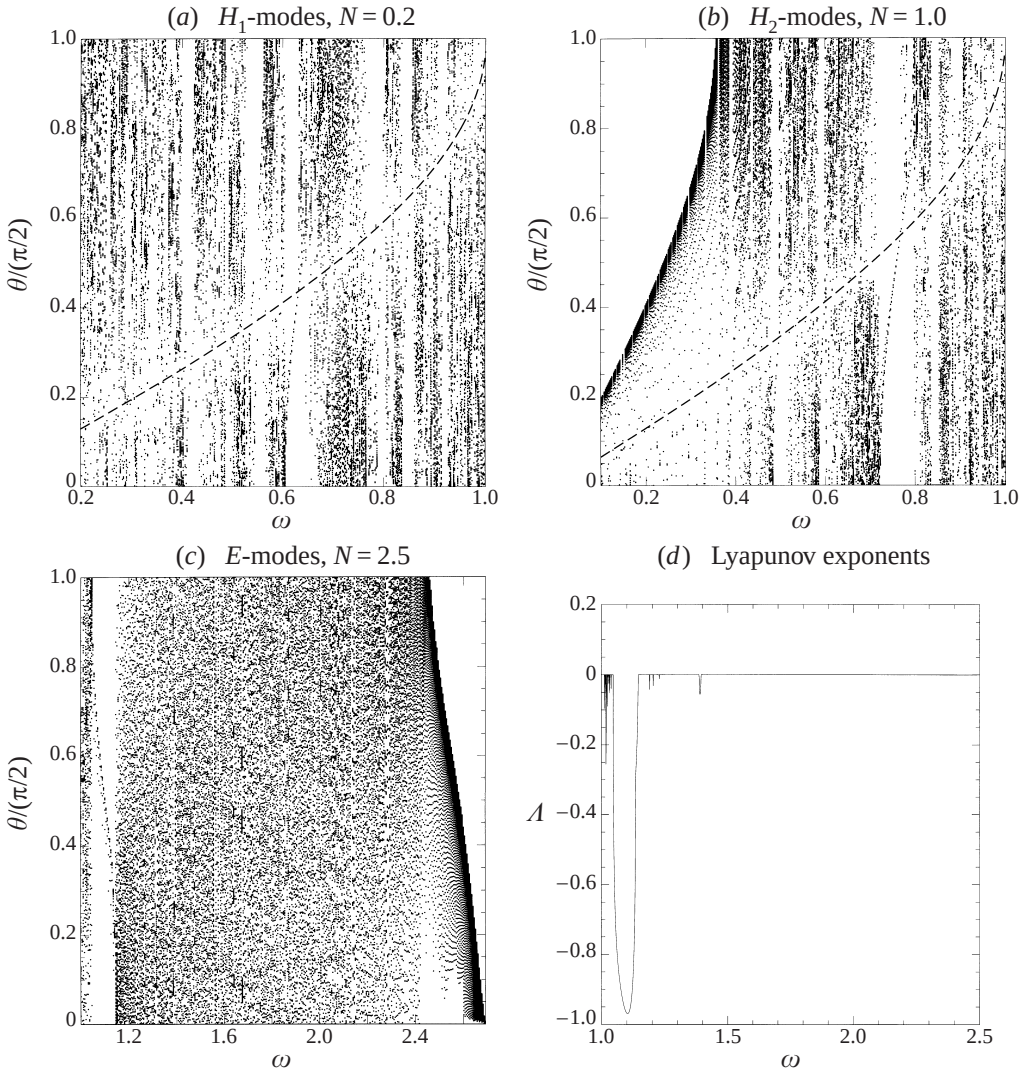

FIGURE 2. (a, b) Poincaré diagrams for H-modes: for each value of ω we plot all the colatitudes of reflection points of the orbit on the inner sphere; for legibility we plot only a hundred points per frequency. Note the absence of reflections near the critical latitude emphasized by a dashed line; such a latitude acts as a repellor as noticed by Maas & Lam (1995). Most of the trajectories seem quasi-periodic except those confined in some limit cycle bands. In (b), a clear accumulation of points denotes the presence of a wedge formed by the turning surfaces and the inner sphere. (c) Poincaré diagrams for E-modes with a hundred reflections on the outer sphere. A large band of periodic orbits with $1.046 \lesssim \omega \lesssim 1.145$ appears but quasi-periodic orbits are still the most numerous. (d) The Lyapunov exponent clearly exhibits the bands of periodic orbits. The absence of points at frequencies $2.4 \lesssim \omega \lesssim N$ is an artefact of plotting, for E_1-characteristics are quasi-focused near the pole since the turning ellipsoid is almost tangent to the outer sphere.

3.1.2. *Paths of characteristics*

A simple way to investigate the properties of solutions of the inviscid equations is to compute the paths of characteristics in the fluid's volume. Such an approach has also been considered by Maas & Lam (1995) in the case of internal gravity waves confined in a two-dimensional parabolic basin.

The paths of characteristics, as shown by figure 1, may be better represented by a map $\theta_{n+1} = f(\theta_n)$ where θ_n is the colatitude of the nth reflection point. Contrary to the case treated by Maas & Lam, however, no analytical expression is known for our maps which are, in addition, not continuous functions for H-modes. The representation with Poincaré diagrams appears to be the most convenient one. The four different cases are illustrated in figure 2.

The first result shown by these figures is the dominance of very long-period orbits for which reflection points seem to be distributed over all angles. Such orbits may also be quasi-periodic or ergodic and therefore may never close. The distinction between very long-period orbits and ergodic ones is difficult numerically. In fact, one can never be sure, using numerical calculations, that an orbit is of ergodic type, because of the finite precision of the computation. Nevertheless, we found, as did Maas & Lam (1995), that the Lyapunov exponent, defined along a trajectory by

$$\Lambda_{\mathcal{N}} = \frac{1}{\mathcal{N}} \sum_{n=1}^{\mathcal{N}-1} \ln \left| \frac{\mathrm{d}\theta_{n+1}}{\mathrm{d}\theta_n} \right| \tag{3.5}$$

is a good indicator of both (i) the period of the final orbit and (ii) the transient of reflections needed to reach this orbit.

The first point is illustrated by figure 2(d), which gives Lyapunov exponents for the E-modes with $N = 2.5$. Some bands of periodic orbits with negative Lyapunov exponents clearly emerge, especially the ones for frequencies such that $1.046 < \omega < 1.145$. We observe the correspondence between these bands of periodic orbits and the narrow vertical white ones in the Poincaré diagram 2(c). Moreover, the similar white bands appearing in the Poincaré diagrams 2(a) and 2(b) also correspond to periodic orbits. It is worth noting that these periodic orbits are all strong attractors with $\Lambda < 0$ while other systems, like gravity modes in a rectangular or semi-elliptic basin, have periodic orbits with $\Lambda = 0$ (see Maas & Lam 1995). In our case we did not detect such orbits, however. A unique period P (defined as the number of reflections from the outer sphere) is associated with each of these bands. We obtain $P = 1$ for the band near $\omega \sim 1.1$ with $\Lambda_{min} \simeq -0.97$, $P = 2$ for those at $\omega \sim 1.4$ with $\Lambda_{min} \simeq -5.57 \times 10^{-2}$ and $P = 4$ for those at $\omega \sim 1.2$ with $\Lambda_{min} \simeq -1.12 \times 10^{-2}$.

In fact, the low absolute value of the Lyapunov exponents outside these bands of frequencies may be understood by plotting the function $\ln|\mathrm{d}\theta_{n+1}/\mathrm{d}\theta_n|$. As shown in figure 3($a$), a very long-period orbit results from the almost perfect matching between contracting intervals (i.e. intervals where $\ln|\mathrm{d}\theta_{n+1}/\mathrm{d}\theta_n| < 0$) and expanding ones. In this case, computing the corresponding Lyapunov exponent along a trajectory from its definition (3.5) is not possible because of the extreme slowness of the convergence of the series. However, assuming the θ_n are evenly distributed in $[0, 2\pi]$ for such orbits, an estimation of Λ may be obtained from

$$\Lambda \sim \frac{1}{2\pi} \int_0^{2\pi} \ln f' \mathrm{d}\theta$$

where f' is the map derivative. For a very long orbit, such as that of figure 3(a), we find $\Lambda \sim 5 \times 10^{-4}$. Since $\ln f' \sim -5 \times 10^{-2}$, the value of the integral clearly shows the almost perfect compensation between contracting and expanding intervals. This situation contrasts strongly with the short-period orbits, such as the one of figure 3(b), where contracting intervals get the better of the expanding ones, leading to a rapid convergence. Fortunately, the above mentioned difficulties for long-period orbits are, however, of little consequence to the physics of the corresponding modes

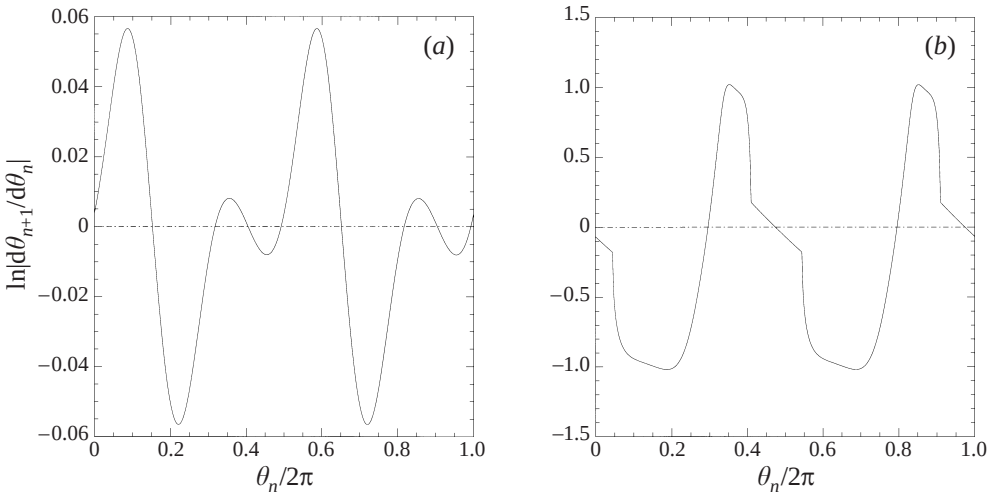

FIGURE 3. Logarithm of the map derivative for a very long-period orbit with $\omega = 1.500$ (*a*) and for a periodic orbit with $\omega = 1.103$ (*b*).

as will be shown below (§ 3.2.2); since no practical difference will appear between long-period orbits and quasi-periodic ones, we shall call quasi-periodic orbits all those with $|\Lambda| \lesssim 10^{-4}$.

The second result shown by plots in figure 2 is the trapping of characteristics by the wedge formed by the intersection of the turning surfaces and the boundaries. This convergence of characteristics in a wedge is systematic for E_2-modes and may occur for H_2-modes. This phenomenon has been noticed several times in the past with either pure internal or inertial waves (see Wunsch 1969; Greenspan 1969). For E_2-modes, the wedge is located on the outer sphere at a latitude ϑ_w given by

$$\sin \vartheta_w = \frac{\omega}{N}\sqrt{1 + N^2 - \omega^2}. \tag{3.6}$$

This wedge exists for all E_2-modes and characteristics are always trapped by it.

For H_2-modes, a 'trapping wedge' is formed only when the apex of the hyperboloidal turning surface is inside the inner shell, i.e. when

$$\omega \leqslant \eta N.$$

As a consequence, if $\eta N > 1$, all H_2-modes face a trapping wedge in the hyperbolic domain. In such a case, it is worth asking whether or not any characteristic in the hyperbolic domain will end in the wedge as for E_2-modes. The answer is no: contrary to the case of E_2-modes, some periodic orbits can coexist with the wedge, as is illustrated by figure 1(*c*); of course no quasi-periodic orbit exists.

The existence of periodic orbits together with the presence of a trapping wedge may be understood easily if one notes that trapping occurs only if the characteristics hit the inner shell at a latitude greater than the critical one, as demonstrated in Appendix A. As may be surmised, the probability of trapping (or the cross-section of the wedge) is an increasing function of the angle made by the apex of the wedge and the critical latitude; this angle is given by

$$\delta\theta = \arcsin\left(\omega\sqrt{1 + \frac{1-\omega^2}{(\eta N)^2}}\right) - \arcsin\omega. \tag{3.7}$$

We note that $\delta\theta \to 0$ as $N \to \infty$ which means that the probability of trapping decreases as stratification increases.

To summarize the behaviour of characteristics, we note that they either converge toward an attractor, which may be a periodic orbit or a wedge formed by the turning surfaces and the boundaries, or wander indefinitely on a quasi-periodic orbit. We shall now investigate the corresponding eigenmodes by solving the equations that include viscosity and thermal diffusion.

3.2. *Gravito-inertial modes with diffusion and viscosity*

To present the structure of eigenmodes, we show, as in paper I, plots of kinetic energy (E_k) and viscous dissipation (D_{visc}), and we complement those by plots of potential energy (E_{th}) and thermal dissipation (D_{th}); these latter quantities give a good representation of the temperature field. The expressions for these quantities are given by

$$\left.\begin{aligned} E_k &= \tfrac{1}{2}u^2, \qquad D_{visc} = \tfrac{1}{2}E\left[s_{rr}^2 + s_{\theta\theta}^2 + s_{\phi\phi}^2 + 2(s_{r\theta}^2 + s_{r\phi}^2 + s_{\theta\phi}^2)\right], \\ E_{th} &= \tfrac{1}{2}\Theta^2, \qquad D_{th} = \frac{EN^2}{\mathscr{P}}|\nabla\Theta|^2, \end{aligned}\right\} \tag{3.8}$$

where s_{ij} are the components of the rate-of-strain tensor in spherical coordinates (r, θ, ϕ).

3.2.1. *H-modes*

Figures 4(*a*) and 4(*b*) show two *H*-modes, one being associated with the attractor (periodic orbit) displayed in figure 1(*d*). The agreement between the inviscid and viscous patterns is fascinating. The thickness of the pattern is a combined effect of viscosity and thermal diffusion and is controlled by the largest of these two parameters. As will be shown below, the structure of the rays is nested shear layers.

A dark line starting near the critical latitude appears on the plots of the temperature fluctuations. This is a property of the reflection of such waves which prevents the radial propagation of characteristics from the critical latitude (Phillips 1963). As the velocity is essentially parallel to the characteristics, and as $\Theta \propto u_r$, the temperature plots show the absence of radial velocity at the critical latitude.

Figure 5(*a*) displays the eigenfunction of a mode for which characteristics are trapped in a wedge formed by the hyperboloid and the inner shell. We note the concentration of the eigenfunction near the wedge. Such a mode is also very strongly damped due to the high spatial frequencies generated by the converging characteristics.†

H-modes corresponding to a quasi-periodic orbit in a shell seem to be very close to pure inertial modes associated with such orbits; they show a dense web of rays which we associate with the propagation of the critical latitude singularity along the characteristics (see figure 5*c*). We think that such modes illustrate the problem examined by Stewartson & Rickard (1969): characteristics following a quasi-periodic orbit scan the whole domain and therefore cannot avoid touching the critical latitude. As shown by Stewartson & Rickard, an integrable singularity in the velocity field develops and propagates everywhere in the shell. The scale and the amplitude are of course bounded by diffusive effects. Note, however, that the results of Stewartson & Rickard were obtained in the case of non-axisymmetric modes in the thin shell limit.

† A wave propagating towards the wedge experiences an increase in wavenumber at each reflection implying a divergence of scale at the wedge position.

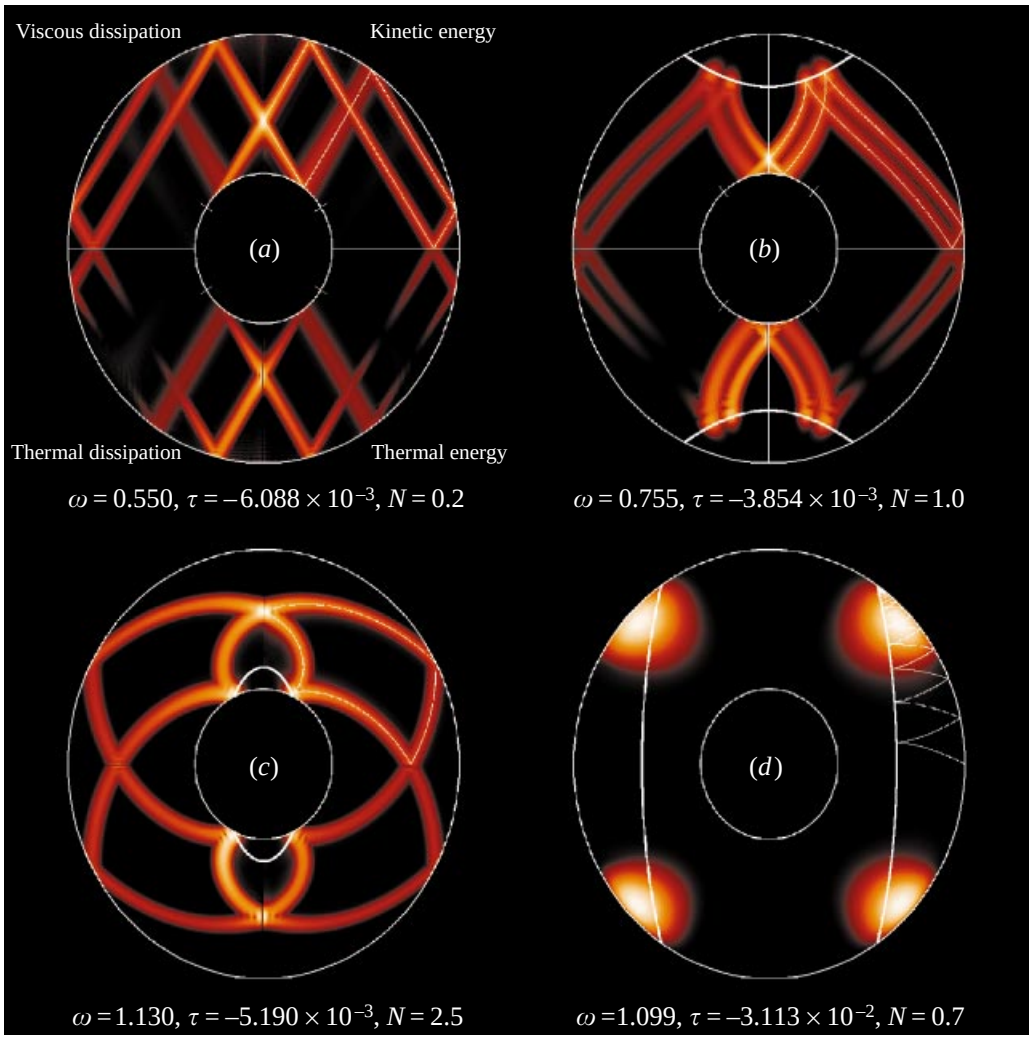

FIGURE 4. (*a*) H_1-mode with $N < \omega < 1$. (*b*) H_2-mode with $0 < \omega < \min(1, N)$. (*c*) E_1-mode with $1 < \omega < N$. (*d*) E_2-mode with $\max(1, N) < \omega < \sqrt{1 + N^2}$. The white path superimposed on the kinetic energy plot corresponds to the characteristic trajectory. For each plot $\mathscr{P} = 1$ and $E = 10^{-7}$ except $E = 5 \times 10^{-6}$ for (*d*).

We believe however that their result extends to axisymmetric modes. Axisymmetric modes in a thin shell do not exist at zeroth order (in thickness of the shell) if the frequency is not vanishing; they therefore require terms of higher order to be dealt with. Stewartson & Rickard did not consider such terms, as their calculation would be more complex, but it is likely that they possess the same type of singularity. When the shell's thickness is of order unity, no difference should be visible in this respect between axisymmetric and non-axisymmetric modes.

3.2.2. *E-modes*

E-modes display the same kind of patterns as *H*-modes but with noticeable differences, however. Among the similarities we observe very spectacular E_1-modes tracing periodic orbits with shear layers (figure 4*c*) as well as E_2-modes with the energy

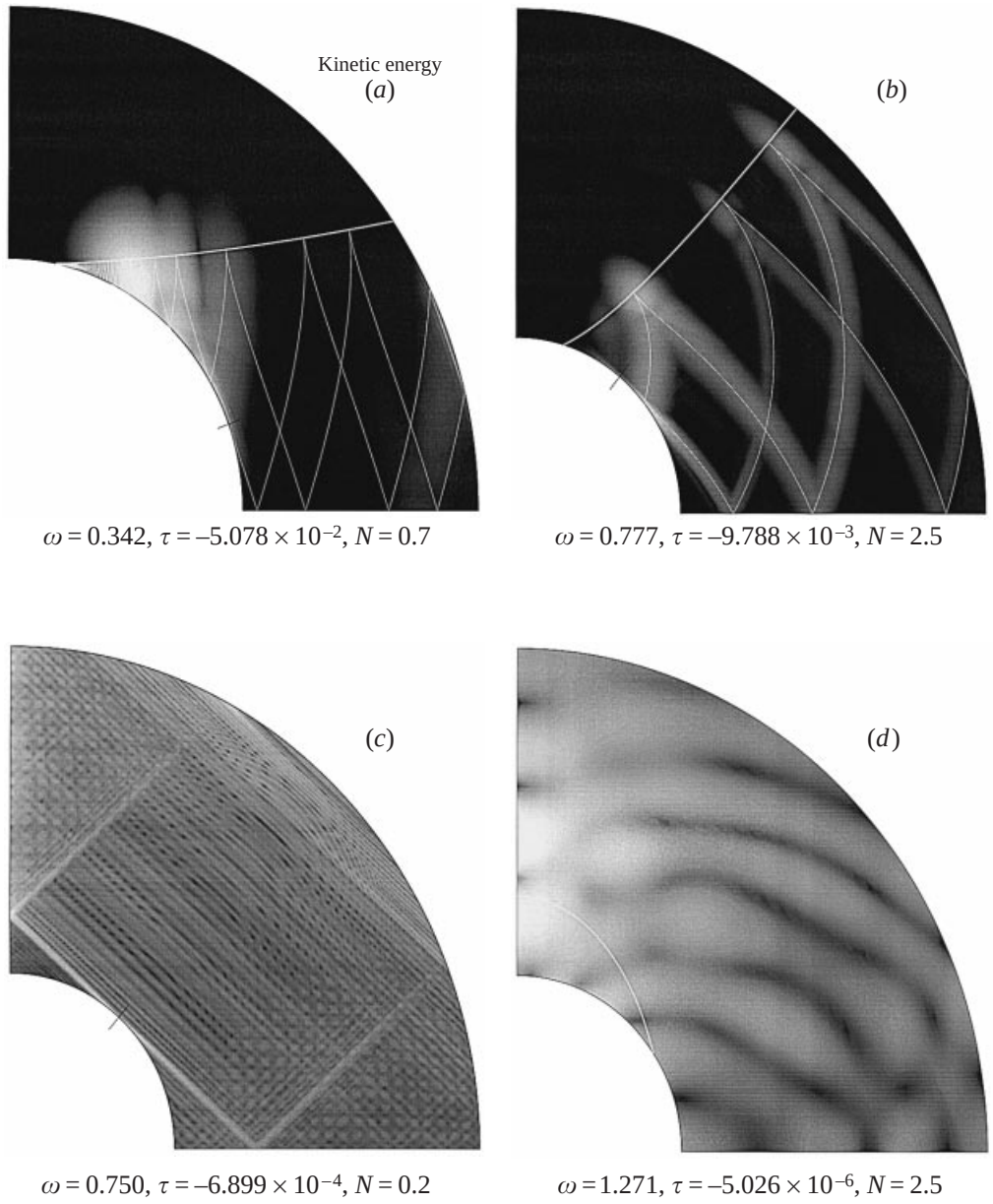

FIGURE 5. (*a*) An H_2-mode associated with characteristics trapped in a wedge on the inner shell ($\eta = 0.5$, $E = 10^{-6}$). (*b*) An H_2-mode associated with an attractive periodic orbit; note the existence of a wedge ($E = 10^{-7}$). (*c*) An H_1-mode associated with a quasi-periodic orbit ($E = 10^{-8}$). (*d*) A regular E_1-mode associated with a quasi-periodic orbit ($E = 10^{-8}$); note the difference in scale with the mode in (*c*). For all the modes $\mathscr{P} = 1$. The resolution for singular modes (a, b, c) is $L = 310, N_r = 150$ and $L = 80, N_r = 60$ for the regular mode (*d*).

concentrated near the wedge formed by the turning surface and the outer sphere (figure 4*d*). However, an important difference appears for modes associated with quasi-periodic orbits. Such modes display large-scale patterns which are independent of the diffusive properties of the fluid: they remain almost unchanged when

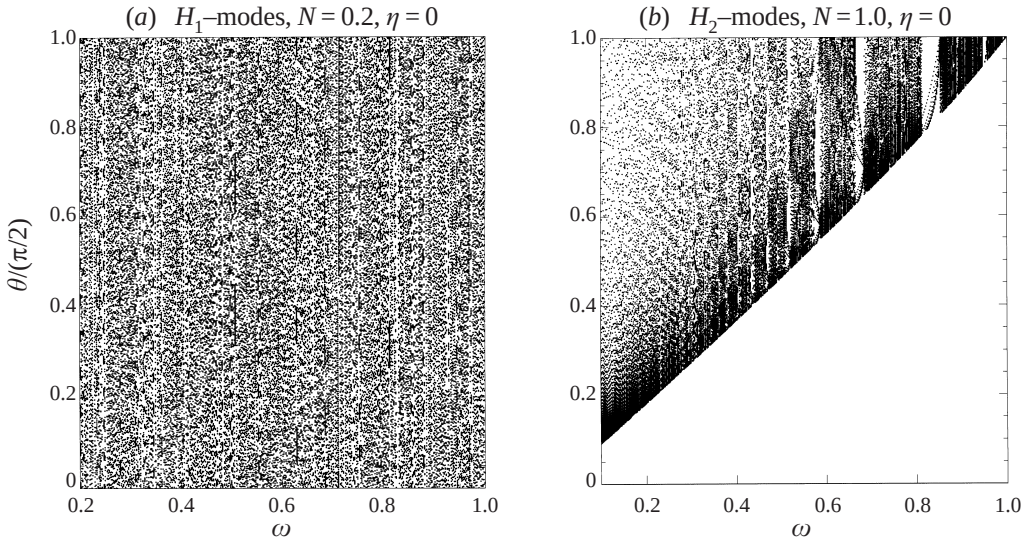

FIGURE 6. Poincaré diagrams of H-modes in the stratified full sphere. About two hundred reflections from the sphere for the H_1-modes and on the turning hyperboloids for H_2-modes have been used. All H_1-modes seem quasi-periodic, which permits the existence of regular solutions. Some limit cycle bands appear with the H_2-modes still leading to a mixing of regular and singular solutions.

the perfect fluid limit is taken. As a consequence, these modes are always the least damped of the whole spectrum. These properties contrast strongly with the equivalent H-modes which display very small scales and are therefore more strongly damped. We interpret this difference as the consequence of the disappearance of the following two constraints: first, the absence of a critical latitude means that the eigenfunction does not have to cope with any singularity; second, no focusing along an attractor occurs. Therefore, they may remain smooth even at zero viscosity (see figures 5*c*, 5*d*). Of course, this conclusion needs to be modified if the orbit is an attractor of very long period. In this case the zero viscosity limit is not smooth, but we conjecture that the effects of the map will be noticeable only when the viscosity is small enough that shear layers along characteristics do not interact. Since such shear layers scale with $E^{1/4}$, very long orbits with, say, a period of 10^5 will appear if the Ekman number is less than 10^{-20} which is (astro)physically irrelevant. From the numerical point of view, the use of a finite resolution (less than 10^5) makes the map invisible for numerical solutions of the inviscid equations. As these solutions remain on large scales, they differ very slightly from their viscous counterparts (as long as the Ekman number is larger than 10^{-20}). For these reasons, we think that a distinction between quasi-periodic orbits and very long-period ones is physically irrelevant.

3.2.3. *The full sphere*

When $\eta = 0$, it has been well known since the work of Bryan (1889) that pure inertial modes exist when viscosity is set to zero. We give some results here which describe the structure of the modes when stratification is included and which further illustrate the mechanisms we have described above for the relation between characteristics orbits and the shape of the eigenfunctions.

It may be shown that for the full unstratified sphere, periodic orbits are such that $\omega = \sin(p\pi/q)$ with p and q integers, while quasi-periodic orbits are associated

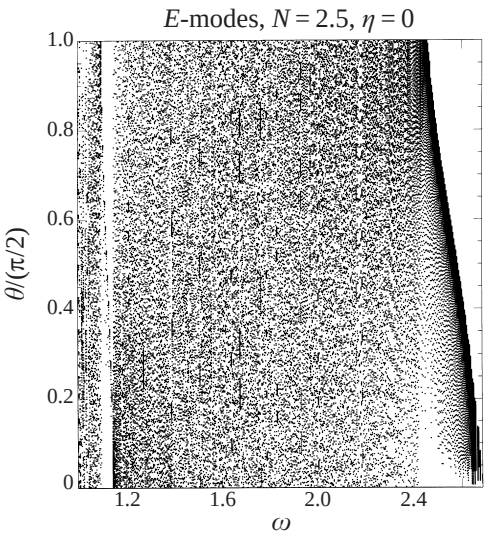

FIGURE 7. Poincaré plot for E-modes in a stratified full sphere; note the frequency band of periodic orbits $1.096 \lesssim \omega \lesssim 1.146$ as in the shell; note however that the band is narrower.

with irrationals r such that $\omega = \sin(r\pi)$. One may also show that the least-damped axisymmetric inertial mode (with $\omega = \sqrt{3/7}$) is associated with a quasi-periodic orbit, but we think that this is true for most of the modes. Hence, pure inertial modes give a good example of the association of quasi-periodic orbits with regular modes.

When a stratification is imposed, most of the modes remain regular. This may be seen on Poincaré maps of figures 6 and 7 where quasi-periodic orbits appear to be the most numerous. When the spatial structure of the modes associated with such orbits is computed, they indeed appear as perfectly regular functions. The critical latitude on the outer sphere does not generate a singularity as this latitude cannot be reached by a grazing characteristic.

However, as shown by Poincaré maps, periodic orbits also exist in some narrow bands and, as in the shell case, they are associated with singular modes whose energy concentrates along the orbit. In the same way, trapping of E_2-modes in a wedge remains in the full sphere case, thus there is no change concerning singular modes in comparison with the shell case.

3.3. *Spectra*

We now briefly turn to the spectral aspect of gravito-inertial modes, and for this purpose we have computed, using the QZ algorithm, the whole spectrum of the discretized equations (2.7) for different stratifications, N.

Figure 8 presents the eigenvalue distributions in the complex plane $(\omega, E\tau^{-1})$; it clearly shows the four spectral bands (3.2) and (3.3) as well as the bounding of frequencies by $\sqrt{1+N^2}$. H_1-modes and E_2-modes only exist for Brunt–Väisälä frequencies of the order of the Coriolis frequency (i.e. when $N \sim 1$); for large stratifications (or slow rotations), the spectrum is dominated by gravity modes slightly perturbed by rotation (E_1-modes).

The case of large stratifications $N \gg 1$ is further illustrated by figure 9. In this figure the asymptotic spectrum for $N = \infty$ is superposed on spectra with increasing stratification. It is clear that the difference between each pair of spectra is important for low-frequency modes, as expected. It also shows that rotation can be considered

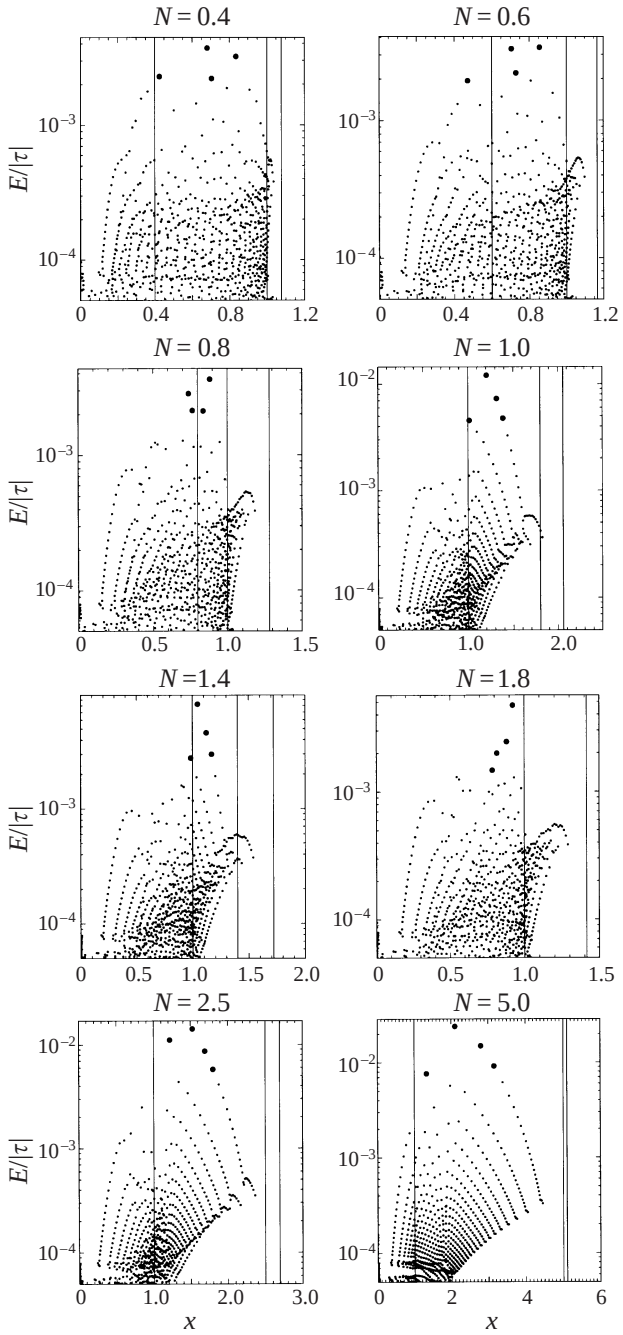

FIGURE 8. Variations of the eigenvalues distribution with the Brunt–Väisälä frequency N ($E = 10^{-5}$ and $\mathscr{P} = 1$); the resolution is $L = 50$ and $N_r = 40$. The solid vertical lines mark the limits of the hyperbolic and elliptic intervals given by (3.2) and (3.3). The thick dots emphasize the four least-damped modes. In each figure, approximatively 700 eigenvalues are plotted.

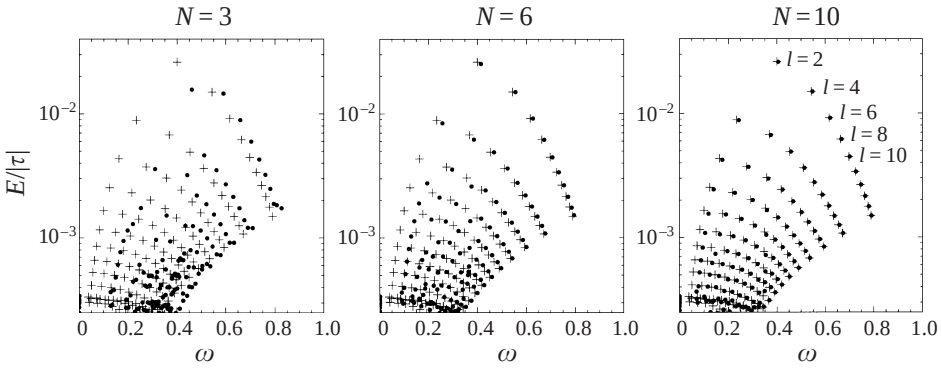

FIGURE 9. Distributions of eigenvalues in the complex plane with rotation(•) and without rotation(+) for different N, frequency being rescaled between $[0, 1]$, $E = 10^{-5}$ and $\mathscr{P} = 1$. This figure shows the ordering of eigenvalues in families as the stratification is increased. Each family emphasizes a branch with fixed ℓ of the dispersion relation $\omega_{\ell,n}$.

as a perturbation for large-scale gravity modes only if $2\Omega/N \lesssim 0.1$. We also see the difference between the spectrum of a separable operator (for pure gravity modes) where eigenvalues are well organized in families corresponding to a specific 'quantum number' (the number of nodes in one direction) and the spectrum of a non-separable operator where eigenvalues seem randomly distributed.

One may wonder now how the behaviour of characteristics appears in the distribution of eigenvalues in the complex plane. Obviously, quasi-periodic orbits associated with regular modes constitute the least-damped part of the spectrum and, as shown by figures 8 and 9, the regular part of the spectrum. Periodic orbits are associated with modes featuring a thin shear layer: they will be associated with eigenvalues with large damping rate. Therefore, if we consider the frequency bands appearing in Poincaré maps, we should find corresponding spectral bands in the complex plane. This is indeed what happens, as nicely shown by figure 10: the largest bands of periodic orbits centred on $\omega = 0.8$ or $\omega = 1.1$ clearly appear as sets of eigenvalues with real parts much larger than those of neighbouring regular modes. Other bands of periodic orbits also exist, but as they are narrower they appear only if the viscosity is low enough.

Finally, modes corresponding to orbits of characteristics trapped by a wedge are also strongly damped like those associated with periodic orbits; in figure 8, E_2-modes may be easily identified.

3.4. *The asymptotic laws*

We now turn to one of the main questions arising in this subject, i.e. the asymptotic behaviour of gravito-inertial modes as the Ekman number or the Prandtl number tends to zero. We recall that typical numbers in radiative zones of stars are $E \sim 10^{-16}$ and $\mathscr{P} \sim 10^{-8}$.

A convenient way to deal with this problem is to study the asymptotic behaviour of the damping rate τ as the Ekman number (or the Prandtl number) is decreased. We recall that (see Appendix B)

$$\tau = -\frac{\mathscr{D}_{th} + \mathscr{D}_{visc}}{2(\mathscr{E}_k + \mathscr{E}_{th})} = -\frac{E}{2}\frac{\displaystyle\int_{(V)} (s_{ij})^2 \mathrm{d}V + (N^2/\mathscr{P})\int_{(V)} (\nabla\Theta)^2 \mathrm{d}V}{\displaystyle\int_{(V)} u^2 \mathrm{d}V + N^2 \int_{(V)} \Theta^2 \mathrm{d}V}. \tag{3.9}$$

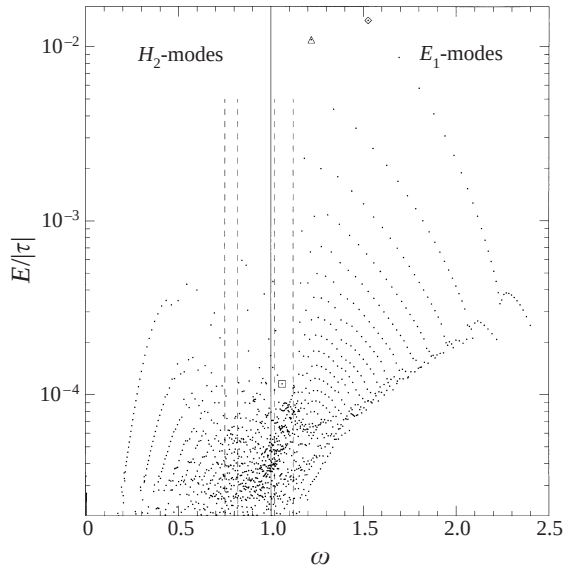

FIGURE 10. Same as figure 8 with $N = 2.5$, $E = 10^{-6}$ and a larger resolution $L = 60$ and $N_r = 60$. Approximately 1200 eigenvalues are plotted. The solid line $\omega = 1$ separates the H_2- and E_1- regions. The dotted lines correspond to limit cycle bands; note the one around $\omega \sim 1.1$ which has already appeared in the Poincaré plot 2(*c*). Symbols mark eigenvalues discussed in figures 12, 14 and 16.

3.4.1. *The limit $E = 0$ at Prandtl number unity*

The easiest case to deal with is that of regular modes. For sufficiently small Ekman numbers the structure of eigenfunctions is independent of viscosity. This point is well illustrated by the mode displayed in figure 11: as the Ekman number is decreased by four orders of magnitude the structure of the mode is hardly changed. In fact, the mode at $E = 0$ can be computed using a mild resolution. As expected and clearly shown by figure 12, the frequency tends to a limiting value ω_0 while the damping rate scales linearly with the Ekman number. Of course, as discussed in § 3.2.2, if the corresponding orbit is not strictly quasi-periodic, ω_0 may not be the true limit but the disappearance of the smooth solution may occur at such a low Ekman number that it is not physically relevant.

If we now consider modes associated with periodic orbits, things are more involved. A pedagogical mode is displayed in figure 13: such a mode features a shear layer centred on a one-loop periodic orbit. Quite clearly (see figure 14) its damping rate follows a power law $\tau \sim E^{\alpha}$ with $\alpha \sim 0.34$, while its frequency seems to tend toward an asymptotic value $\omega_0 \sim 1.05$. This behaviour is easily understood when one examines the structure of the shear layers: nested shear layers appear with scale close to $E^{1/3}$ and $E^{1/4}$, which are reminiscent of Stewartson layers (see Appendix C for a demonstration).

However, the value of the exponent close to one third may just be fortuitous since other modes show different value, as shown by figure 15. In this figure it is clear that as the viscosity decreases eigenvalues interact in the complex plane. Such interactions result from the fact that exponents of damping rates are different while eigenfrequencies change very little with the Ekman number. For a pair of eigenvalues of similar imaginary parts, an Ekman number exists where damping rates will also be very similar, implying a strong interaction between the two eigenvalues; this usually

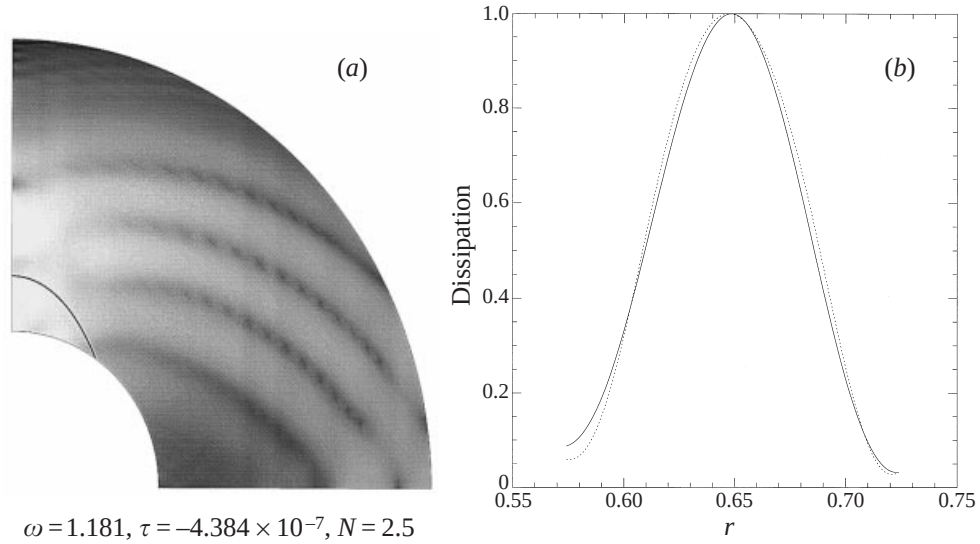

FIGURE 11. (*a*) Viscous dissipation of the E_1-mode of figure 12 with $E = 10^{-9}$ and $\mathscr{P} = 1$. (*b*) radial profiles of the viscous dissipation at the colatitude $\theta = 40^\circ$ for $E = 10^{-5}$ (solid line) and $E = 10^{-9}$ (dotted line): the width of the pattern remains constant.

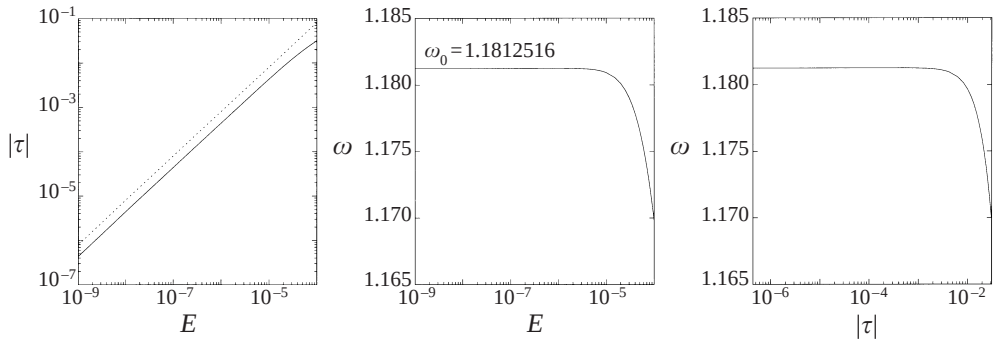

FIGURE 12. Evolution of $|\tau|$ and ω as E diminishes with $\mathscr{P} = 1$ for the regular E_1-mode marked by a triangle in figure 10. The frequency slowly tends to its asymptotic inviscid value $\omega_0 = 1.1812516$. The dotted line corresponds to the law $|\tau| \propto E$.

leads to an exchange of eigenvectors. Such events, illustrated by figure 15, tend to support the idea, first raised in paper I, that modes may 'bifurcate' continually as viscosity tends to zero and that no limit exists. Contrarily, figure 14 would support the existence of a limit, such a limit being that the eigenmode at zero viscosity is non-zero only on the line drawn by the periodic orbit. We may reconcile these two behaviours if we admit that the successive bifurcations are in fact only a 'transient' and that in the case of figure 15 the asymptotic régime has not been reached yet.

Finally, modes trapped by a wedge show damping rates decreasing with the Ekman number with a law compatible with $E^{1/3}$. We surmise that this behaviour illustrates the fact that, as for inertial modes, the smallest scale of the velocity field is $O(E^{1/3})$.

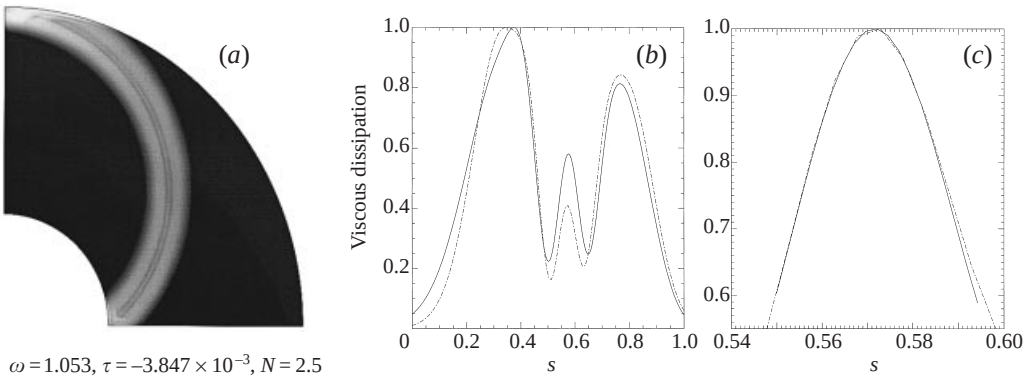

FIGURE 13. (*a*) Shape of the eigenfunction associated with the E_1-mode examined in figure 14. Viscous dissipation is represented at $E = 10^{-7}$ and $\mathscr{P} = 1$. (*b*) Profiles of the viscous dissipation at $z \simeq 0.5$ for $E = 10^{-6}$ (solid line) and $E = 10^{-7}$ (dotted line). There are three overlapping shear layers with different scalings. (*c*) A zoom of the central layer shows a scaling exponent of 0.31 (the scale for the dotted line was increased by a factor $(10^{-6}/10^{-7})^{0.31}$) while two other layers show a scaling exponent close to $\frac{1}{4}$.

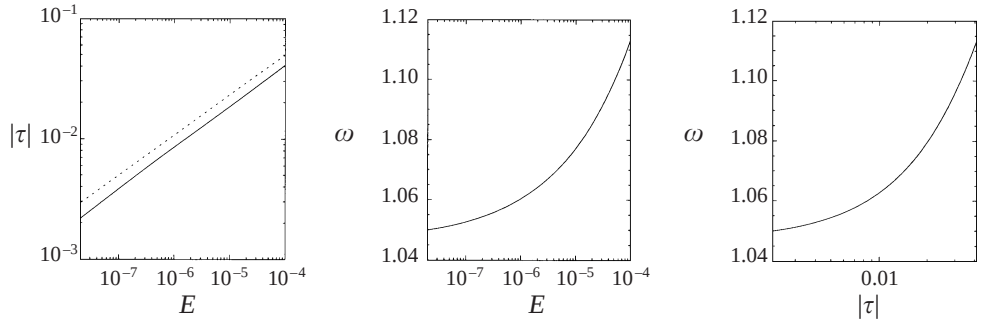

FIGURE 14. Same as figure 12 with $\mathscr{P} = 1$ but for the singular E_1-mode marked by a square in figure 10. The dotted line corresponds to the law $|\tau| \sim E^{1/3}$.

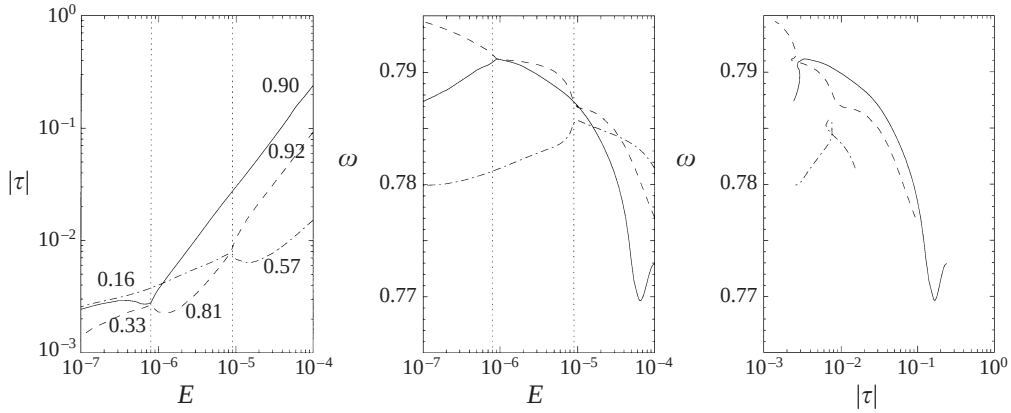

FIGURE 15. Paths of three H_2-eigenvalues in the complex plane for $N = 1$. The dotted lines mark the modes' interactions at $E = 8 \times 10^{-6}$ and $E = 8 \times 10^{-7}$. The numbers labelling the curves on the $|\tau|$ versus E plot are the exponents a of the closest power law $|\tau| \sim E^a$.

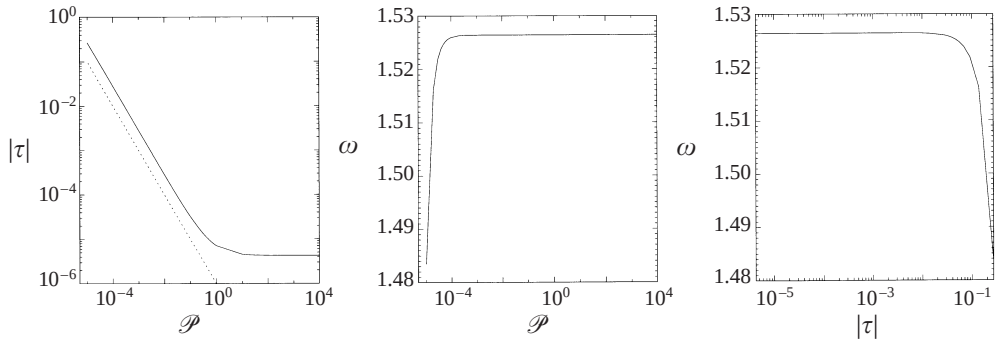

FIGURE 16. Evolution of $|\tau|$ and ω versus $\mathscr{P}$ with $E = 10^{-7}$ and $N = 2.5$ for the least-damped E_1-mode marked by a diamond in figure 10. The dotted line corresponds to the law $|\tau| \sim \mathscr{P}^{-1}$.

3.4.2. *Varying the Prandtl number*

In order to have a first impression of the effects of varying the Prandtl number, we computed the path in the complex plane of the eigenvalue corresponding to the least-damped mode when $E = 10^{-7}$ and $N = 2.5$. The Prandtl number was varied between 10^{-5} and 10^4. As shown by figure 16, the case $\mathscr{P} = 1$ is very close to the asymptotic limit $\mathscr{P} = \infty$. In this limit, which finds applications in ocean dynamics, dissipation is only due to viscosity.

When stars are considered, the interesting limit is $\mathscr{P} = 0$. However, one always has $E \ll \mathscr{P} \ll 1$ which means that the main contribution to the damping rate is due to heat diffusion. Figure 16 shows that as the Prandtl number is decreased, the damping rate first increases as $\mathscr{P}^{-1}$ as expected for a regular mode, while the frequency remains constant. When $\mathscr{P} \sim 5 \times 10^{-5}$ the frequency changes dramatically. We think that this is the start of a new régime where $\mathscr{P} \lesssim E \ll 1$. In such a range of parameters, eigenvalues are distributed into two kinds of families: pure inertial modes and pure thermal modes. This corresponds to the decoupling of the temperature equation and the dynamic equation:

$$\left.\begin{aligned} &\lambda \boldsymbol{u} + \boldsymbol{e}_z \wedge \boldsymbol{u} = -\nabla\pi + E\Delta\boldsymbol{u}, \\ &\lambda\Theta \simeq (E/\mathscr{P})\Delta\Theta. \end{aligned}\right\} \tag{3.10}$$

We shall not consider this case any further.

An interesting remark may be made in the case $E \ll \mathscr{P} \ll 1$: as heat diffusion is the main diffusive effect, it suggests that setting the Ekman number to zero while keeping $E/\mathscr{P}$ finite is an efficient way of dealing with such a range of parameters. In the case of regular modes this is obviously true, but this also happens to be true for E_1-modes associated with a limit cycle. However, singular H-modes cannot be computed with this limit; we shall develop this point in a future paper.

4. Discussion

4.1. *Gravito-inertial modes*

The numerical results we have presented in the preceding section enable us to have a glimpse of what could be the shape of the spectrum at (or close to) the zero diffusivity limit ($\nu = \kappa = 0$).

4.1.1. *Regular modes*

Regular modes are those for which the velocity field remains square-integrable and continuous. They are associated with a discrete set of eigenvalues; when the container is a shell their eigenfrequencies seem to be contained in the interval [1, N] from which subintervals corresponding to periodic orbits of characteristics have been removed. In the remaining subintervals, eigenfrequencies are likely to be dense. If the container is a full sphere, regular modes may be found for frequencies in [0, N] with the exclusion of some subinterval as above.

All the above numerical results lead us to believe that regular modes are associated with quasi-periodic orbits of characteristics, i.e. orbits for which the Lyapunov exponent is strictly zero. However, the distinction between quasi-periodic orbits and very long-period orbits is impossible numerically. Therefore, 'regular modes' which we observe may be regular only if a slight amount of diffusion is included; we may indeed surmise that the attractor will appear if diffusivities are so low that shear layers associated with the attractors do not overlap. Thus periodic orbits with 10^4 reflection points would not show up as long as the Ekman number (or $E/\mathscr{P}$) is larger than 10^{-16} which is usually the case, even in stars.

It is interesting to note here that for strictly two-dimensional problems, regular modes are associated with periodic orbits of characteristics possessing a zero Lyapunov exponent. Examples given in Maas & Lam (1995) in fact illustrate some mathematical results derived for two-dimensional systems by Bourgin & Duffin (1939), John (1941), Franklin (1972) and Schaeffer (1975). In these systems, eigenvalues are always infinitely degenerate and no velocity field is associated with quasi-periodic orbits. On the other hand, in three-dimensional systems eigenvalues seem to be associated with quasi-periodic orbits and are not degenerate as the full unstratified sphere or the cylinder cases suggest.

4.1.2. *Singular modes trapped in a wedge*

We have also encountered modes for which characteristics are trapped in a wedge formed by the boundaries and the turning surfaces. We expect that such modes will completely disappear in the zero-diffusion case. Indeed, it was shown by Ralston (1973) that when the Poincaré equation is simplified into a wave equation, the set of eigenvalues corresponding to the cases where characteristics are trapped in a wedge (here made by the boundaries) is empty: eigenfunctions are no longer square-integrable. We conjecture that this result can be generalized to our case and that eigenvalues also disappear from the frequency bands corresponding to trapped characteristics. Hence, no eigenvalue should remain in the interval $[N, \sqrt{N^2+1}]$ when $\nu = \kappa = 0$; this also means, in mathematical terms, that the point spectrum of the operator is empty and only singular solutions associated with the continuous band $[N, \sqrt{N^2+1}]$ remain (Dautray & Lions 1984/1985).

4.1.3. *Singular modes associated with periodic orbits*

We now turn to the most interesting modes: those for which the amplitude of the eigenfunction is concentrated along a periodic orbit. For such eigenvalues, the trajectories of characteristics are endowed with a strictly negative Lyapunov exponent so that the associated map is contracting. When diffusion is taken into account, the contracting action of the map is balanced in some way by diffusive effects. The shape of the modes and, more precisely, the thickness of shear layers may be controlled by the value of the Lyapunov exponent.

In the limit $\nu = \kappa = 0$, the eigenfunctions (a distribution in fact) will be restricted to

the line drawn by the periodic orbit. However, such eigenfunctions are in all likelihood not square-integrable. This property may be conjectured from the results of Maas & Lam (1995); in the case investigated by these authors, two-dimensional gravity modes in a parabolic basin, the streamfunction associated with a periodic orbit can be constructed explicitly. Characteristics act as a mapping of an arbitrary function defined on a segment of the boundary. As the characteristics converge towards the attractor, the scale of the function is reduced while its amplitude is conserved. As a result, derivatives of the streamfunction (i.e. components of the velocity field) diverge. Hence, it is clear that the velocity field is not square-integrable and this explains the concentration of kinetic energy along the attractor. On the mathematical side this implies that no eigenvalue exists in bands of frequencies where periodic orbits are present; in other words, the point spectrum of the operator is empty and one is left with the continuous spectrum associated with singular solutions.

4.1.4. *Non-axisymmetric modes*

In the presentation of the results we concentrated on axisymmetric modes only. The generalization of our results to non-axisymmetric modes is straightforward however, if we recall the following two points: first, in a spherical geometry the azimuthal variable ϕ is separable from the two others (r, θ), therefore modes with $e^{im\phi}$ dependence can be computed separately; second, the path of characteristics is independent of m as second-order derivatives do not contain this parameter. Thus singularities which arise because of the focusing of characteristics also appear in the meridional section of non-axisymmetric modes but are modulated by $e^{im\phi}$.

4.2. *Inertial modes*

In view of the preceding conclusions, we may understand somewhat better the results obtained in paper I for pure inertial modes. For such modes, eigenfunctions tracing a periodic orbit are much less evident. Results of paper I gave evidence in favour of the scenario with an infinite suite of bifurcations. In view of the behaviour of gravito-inertial modes, we may interpret our results in the following way: periodic orbits for pure inertial modes appear in rather narrow bands of frequencies, and in such bands the Lyapunov exponent is often small (in modulus); therefore, the asymptotic régime may be reached only at very low values of the Ekman number. The case of pure inertial modes is, quite surprisingly, less obvious than the case of gravito-inertial modes and will be reconsidered in a forthcoming paper.

4.3. *Astrophysical applications*

The above results have straightforward consequences as far as astrophysical applications are concerned. It is clear, for instance, that regular modes will be the best candidates for interpreting the pulsation spectrum of a rapidly rotating star, since least-damped modes will be most easily excited by the driving instabilities. Our results limit the possible identification of observed frequencies or the spectral bands to search for such modes.

Another conclusion concerns the transport properties of gravito-inertial modes. As mentioned in the introduction, waves are expected to play an important role in the radiative zones of stars in transporting angular momentum or chemical elements. As far as angular momentum transport is concerned, waves of frequency close to that of the rotation are most important. Our results show that for this range of frequencies, the spectrum essentially consists of singular modes (associated with periodic orbits) whose damping rate is much larger than that of regular modes. The time scale on

which angular momentum is transferred from one place to another will therefore be very different according to whether a singular or a regular mode is excited. This point will be developed in another forthcoming paper.

As a final conclusion to this paper, we should emphasize that our results, based on numerical experiments, are only conjectures on the mathematical properties of such an eigenvalue problem. We feel, however, that these conjectures can be demonstrated, but this is the subject of future work.

We thank Valerie Frayssé and Jean-Christophe Rioual for letting us use their eigenvalue solver. We also thank Gary Henderson, Leo Maas and Susan Friedlander for their careful reading of the manuscript. We acknowledge many fruitful discussions with our colleagues B. Georgeot, J. Sommeria and B. Valette. Most of the calculations have been carried out on the Cray C98 and Fujitsu VP300 of the Institut du Développement et des Ressources en Informatique Scientifique (IDRIS) which is gratefully acknowledged. The support of the GdR CNRS/IFREMER 1074 (Mécanique des Fluides Géophysique et Astrophysiques) and the EEC 'Human Capital and Mobility' contract No CHRX-CT94-0483 are also gratefully acknowledged.

Appendix A. Wedge focusing

The slope of characteristics of H_2-modes propagating towards a wedge formed by the intersection of the turning hyperboloid and the inner shell are such that

$$\frac{\mathrm{d}z}{\mathrm{d}s} = \frac{zsN^2 - \xi^{1/2}}{\omega^2 - N^2z^2}, \qquad \xi = \omega^2N^2s^2 + (1-\omega^2)(\omega^2 - N^2z^2).$$

Propagation towards the wedge is possible only if

$$\left|\frac{\mathrm{d}z}{\mathrm{d}s}\right|_{char} \geqslant \left|\frac{\mathrm{d}z}{\mathrm{d}s}\right|_{boundary}.$$

As $\mathrm{d}z/\mathrm{d}s < 0$ the above inequality yields

$$\xi^{1/2} - zsN^2 > \left(\omega^2 - N^2z^2\right)\frac{s}{z}.$$

After some algebra, we find the following relation:

$$\left(\omega^2 - N^2z^2\right)\left(\omega^2\eta^2 - z^2\right) < 0$$

which implies that $\omega^2\eta^2 - z^2 < 0$ on the inner boundary. As $z = \eta\sin\vartheta$, this condition is equivalent to

$$\sin\vartheta > \omega \equiv \sin\vartheta_c \quad \Rightarrow \quad \vartheta > \vartheta_c \quad \text{with} \quad \vartheta \in [0, \pi/2] \tag{A 1}$$

where ϑ_c is the critical latitude.

Appendix B. Quadratic quantities

In this Appendix we calculate the local energies and dissipations given by (3.8). We first rewrite the system (2.1):

$$\left.\begin{aligned} &\partial u/\partial t + \boldsymbol{e}_z \wedge \boldsymbol{u} = -\nabla\pi + N^2\Theta\boldsymbol{r} + E\Delta\boldsymbol{u}, \\ &\nabla\cdot\boldsymbol{u} = 0, \\ &\partial\Theta/\partial t + ru_r = (E/\mathscr{P})\Delta\Theta. \end{aligned}\right\} \tag{B 1}$$

Multiplying the Navier–Stokes equation by $\boldsymbol{u}$ and the energy equation by Θ, we find after integration:

$$\frac{\mathrm{d}}{\mathrm{d}t}\left(\int_{(V)}\frac{u^2}{2}\mathrm{d}V+N^2\int_{(V)}\frac{\Theta^2}{2}\mathrm{d}V\right)=-\left(\frac{EN^2}{\mathscr{P}}\int_{(V)}|\boldsymbol{\nabla}\Theta|^2\mathrm{d}V+\frac{E}{2}\int_{(V)}(s_{ij})^2\mathrm{d}V\right)$$

where $s_{ij}=\partial_i u_j+\partial_j u_i$. Let $\mathscr{E}_k=\int_{(V)}\frac{1}{2}u^2\mathrm{d}V$ be the total kinetic energy, $\mathscr{E}_{th}=N^2\int_{(V)}\frac{1}{2}\Theta^2\mathrm{d}V$ be the total potential energy, $\mathscr{D}_{th}=(EN^2/\mathscr{P})\int_{(V)}|\boldsymbol{\nabla}\Theta|^2\mathrm{d}V$ be the total thermal dissipation and $\mathscr{D}_{visc}=\frac{1}{2}E\int_{(V)}(s_{ij})^2\mathrm{d}V$ be the total viscous dissipation, then we have

$$\frac{\mathrm{d}}{\mathrm{d}t}\left(\mathscr{E}_k+\mathscr{E}_{th}\right)=-\left(\mathscr{D}_{th}+\mathscr{D}_{visc}\right) \tag{B 2}$$

which shows that the total energy of the fluid's motion is damped out by the thermal and viscous dissipations. This equation is useful for testing the spectral convergence of eigenvectors since one may check the following relation between the eigenvector and the (real part of the) eigenvalue:

$$\tau=\frac{1}{2\left(\mathscr{E}_k+\mathscr{E}_{th}\right)}\frac{\mathrm{d}}{\mathrm{d}t}\left(\mathscr{E}_k+\mathscr{E}_{th}\right)=-\frac{\mathscr{D}_{th}+\mathscr{D}_{visc}}{2\left(\mathscr{E}_k+\mathscr{E}_{th}\right)}.$$

We note that these quadratic quantities may easily be expressed in terms of the radial functions of the spherical harmonic decompositions of the fields. Using the decompositions (2.4) of $\boldsymbol{u}$ and Θ and the orthogonality relations between $\boldsymbol{R}_\ell^m$, $\boldsymbol{S}_\ell^m$ and $\boldsymbol{T}_\ell^m$, we have

$$\left.\begin{aligned}
E_k&=\tfrac{1}{2}\sum_{\ell,m}\int_\eta^1\left[|u_m^\ell|^2+\ell(\ell+1)\left(|v_m^\ell|^2+|w_m^\ell|^2\right)\right]r^2\mathrm{d}r,\\
E_{th}&=\frac{N^2}{2}\sum_{\ell,m}\int_\eta^1|t_m^\ell|^2r^2\mathrm{d}r,\\
\mathscr{D}_{th}&=\frac{EN^2}{\mathscr{P}}\sum_{\ell,m}\int_\eta^1\left[\left|\frac{\partial t_m^\ell}{\partial r}\right|^2+\frac{\ell(\ell+1)}{r^2}|t_m^\ell|^2\right]r^2\mathrm{d}r,\\
\mathscr{D}_{visc}&=E\sum_{\ell,m}\int_\eta^1\left[3\left|\frac{\partial u_m^\ell}{\partial r}\right|^2+\ell(\ell+1)\left(|a_m^\ell|^2+|b_m^\ell|^2\right)\right.\\
&\qquad\left.+\ell(\ell^2-1)(\ell+2)\left(|v_m^\ell|^2+|w_m^\ell|^2\right)/r^2\right]r^2\mathrm{d}r,
\end{aligned}\right\} \tag{B 3}$$

with $\quad a_m^\ell=\frac{\partial v_m^\ell}{\partial r}+\frac{u_m^\ell-v_m^\ell}{r}\quad$ and $\quad b_m^\ell=r\frac{\partial}{\partial r}\left(\frac{w_m^\ell}{r}\right).$

Appendix C. The scales of shear layers

We show here that the scales of shear layers associated with periodic orbits may be, as for inertial modes, $O(E^{1/3})$ or $O(E^{1/4})$.

We first assume that such shear layers are thicker than Ekman layers, i.e. we assume that their width scales with E^a and $a<\frac{1}{2}$. We also suppose that the Prandtl number is finite. With these assumptions and in the limit of vanishing Ekman numbers, we may neglect the diffusion term in the temperature equation and thus write $\Theta=-ru_r/\lambda$.

Hence the dynamics of gravito-inertial modes is controlled by

$$\left.\begin{aligned} &\lambda \boldsymbol{u} + \boldsymbol{e}_z \wedge \boldsymbol{u} = -\nabla \Pi - (N^2/\lambda) r u_r \boldsymbol{r} + E \Delta \boldsymbol{u}, \\ &\nabla \cdot \boldsymbol{u} = 0. \end{aligned}\right\} \tag{C 1}$$

The form of such equations is similar to that of those controlling the dynamics of inertial modes; the additional term $-(N^2/\lambda) r u_r \boldsymbol{r}$ just changes the shape of characteristics and the size of the hyperbolic domain. Therefore, one should expect that the width of shear layers is the same as for inertial modes since the new term does not contain any derivative of the velocity field.

Let us formulate this reasoning in more mathematical terms. The equation of dynamics may be written as

$$\mathscr{L}(\boldsymbol{u}) = -\nabla P + E \Delta \boldsymbol{u} \tag{C 2}$$

where $\mathscr{L}$ is a linear (but not differential) operator which reads

$$\mathscr{L} = \begin{pmatrix} \lambda + a \sin^2\theta & -1 & a \sin\theta \cos\theta \\ 1 & \lambda & 0 \\ a \sin\theta \cos\theta & 0 & \lambda + a \cos^2\theta \end{pmatrix} \quad \text{with} \quad a = N^2 r^2/\lambda.$$

We restrict our reasoning to axisymmetric modes and we introduce the meridional streamfunction $\psi(s,z)$ such that

$$\boldsymbol{u} = \nabla \times (\psi \boldsymbol{e}_\theta / s) + v(s,z) \boldsymbol{e}_\theta.$$

The θ-component of (C 2) and the θ-component of the curl of (C 2) yield

$$(\lambda - E\Delta') v = \frac{1}{s} \frac{\partial \psi}{\partial z},$$

$$\boldsymbol{e}_\theta \cdot \nabla \times \left\{ \mathscr{L} \left[\nabla \times (\psi \boldsymbol{e}_\theta / s) + v \boldsymbol{e}_\theta \right] \right\} + E \Delta'^2 (\psi/s) = 0,$$

where $\Delta' = \Delta - 1/s^2$. The second equation may be rewritten as

$$\boldsymbol{e}_\theta \cdot \nabla \times \left\{ \mathscr{L} \left[\nabla \times (\psi \boldsymbol{e}_\theta / s) \right] \right\} - \frac{\partial v}{\partial z} + E \Delta'^2 (\psi/s) = 0$$

to which we apply the operator $\lambda - E\Delta'$; hence, it follows that

$$(\lambda - E\Delta') \left[\boldsymbol{e}_\theta \cdot \nabla \times \left\{ \mathscr{L} \left[\nabla \times (\psi \boldsymbol{e}_\theta / s) \right] \right\} \right] - \frac{1}{s} \frac{\partial^2 \psi}{\partial z^2} + E \Delta'^2 (\lambda - E\Delta')(\psi/s) = 0.$$

We now write this equation using characteristics coordinates $u_\pm$ (which are real only in the hyperbolic domain). The inviscid part of this equation is an Euler–Darboux equation of the form

$$\frac{\partial^2 \psi}{\partial u_+ \partial u_-} + f \frac{\partial \psi}{\partial u_+} + g \frac{\partial \psi}{\partial u_-} = 0$$

where f and g are functions of (u_+, u_-); when viscosity is taken into account and when only terms with highest derivatives are retained, then

$$E^2 \frac{\partial^6 \psi}{\partial u_-^6} + \lambda E \frac{\partial^4 \psi}{\partial u_-^4} + \frac{\partial^2 \psi}{\partial u_+ \partial u_-} + f \frac{\partial \psi}{\partial u_+} + g \frac{\partial \psi}{\partial u_-} + \cdots = 0$$

along a characteristic $u_+ = \text{const}$. It is easily seen that a distinguished limit exists if $\psi \equiv \psi((u_- - u_0)/E^{1/3})$. If the variations of $\partial\psi/\partial u_-$, due to inviscid balance along such a characteristic, are taken into account, then a scaling in $E^{1/4}$ also appears (see

below). Therefore, as observed numerically (see figure 13), shear layers associated with limit cycles possess (at least) two length scales: $O(E^{1/3})$ and $O(E^{1/4})$.

We finally note that this result is quite general, as it is independent of the spatial variations of the Brunt–Väisälä frequency.

Appendix D. Addendum to paper I: $E^{1/4}$ shear layers

When studying the structure of pure inertial waves in paper I, it was shown that the thickness of some shear layers scales with $E^{1/4}$; such a scaling was first mentioned by Gans (1983) as a possible alternative to the more familiar $E^{1/3}$ scale. We show below how to derive more directly this other possible scale for internal shear layers.

It is well known that when viscosity is taken into account, pressure perturbations of damped inertial modes obey the general equation

$$E^2\Delta^3 P - 2E\lambda\Delta^2 P + \lambda^2\Delta P + \frac{\partial^2 P}{\partial z^2} = 0 \tag{D 1}$$

where $\lambda = \tau + \mathrm{i}\omega$ as in the rest of the paper. We restrict ourselves to axisymmetric modes and introduce characteristics coordinates $u_\pm = \omega z \pm \alpha r$ with $\alpha = \sqrt{1-\omega^2}$. Noting that $|\omega| \gg |\tau|$ when $E \to 0$, we can rewrite (D 1) as

$$E^2\Delta^3 P - 2E\mathrm{i}\omega\Delta^2 P + \tau 2\mathrm{i}\omega\Delta P + 4\omega^2\alpha^2\frac{\partial^2 P}{\partial u_+\partial u_-} - \frac{2\alpha^2\omega^2}{u_+ - u_-}\left(\frac{\partial P}{\partial u_+} - \frac{\partial P}{\partial u_-}\right) = 0. \tag{D 2}$$

In the case of a ray where $\partial P/\partial u_- \gg \partial P/\partial u_+$, we noted in paper I that the inviscid equation leads to

$$\frac{\partial P}{\partial u_-} = \frac{f(u_-)}{\sqrt{u_+ - u_-}}$$

where f is an arbitrary function with a support scaling with the thickness of the layer.

We now look for a solution of (D 2) which contains this inviscid balance, i.e. with P such that

$$P = \int \frac{f(u_-)\mathrm{d}u_-}{\sqrt{u_+ - u_-}}.$$

Introducing the scaled variable $X = (u_- - u_0)/\delta$ with $\delta \ll 1$ and noting that $P \simeq \delta F(X)/\sqrt{u_+ - u_0}$, the leading-order terms of (D 2) yield

$$\frac{E^2}{\delta^6}\frac{\partial^6 F}{\partial X^6} - \frac{2\mathrm{i}\omega E}{\delta^4}\frac{\partial^4 F}{\partial X^4} + \frac{2\mathrm{i}\omega\tau}{\delta^2}\frac{\partial^2 F}{\partial X^2} + \frac{\alpha^2\omega^2}{(u_+ - u_0)^2}F = 0.$$

Assuming that the damping rate τ scales with E^a, where $a \geqslant \frac{1}{2}$ (as observed numerically), the only distinguished limit is with $\delta = E^{1/4}$.

Hence, it is clear that internal oscillating shear layers are nested boundary layers like steady Stewartson layers.

REFERENCES

Arnoldi, W. E. 1951 The principle of minimized iterations in the solution of the matrix eigenvalue problem. *Q. Appl. Maths* **9**, 17–29.

Balona, L. A., Böhm, T., Foing, B. H., Ghosh, K. K., Janot-Pacheco, E., Krisciunas, K., Lagrange, A.-M., James, S. D., Baudrand, J., Catala, C., Dreux, M., Felenbok, P. & Hearnshaw, J. B. 1996 Line profile variations in γ Doradus. *Mon. Not. R. Astron. Soc.* **281**, 1315–1325.

Bourgin, D. & Duffin, R. 1939 The dirichlet problem for the vibrating string equation. *Bull. Am. Math. Soc.* **45**, 851–859.

Bryan, G. 1889 The waves on a rotating liquid spheroid of finite ellipticity. *Phil. Trans. R. Soc. Lond.* **180**, 187–219.

Chandrasekhar, S. 1961 *Hydrodynamic and Hydromagnetic Stability*. Oxford University Press.

Dautray, R. & Lions, J.-L. 1984/1985 *Analyse Mathématique et Calcul Numérique*. Masson.

Fotheringham, P. & Hollerbach, R. 1998 Inertial oscillations in a spherical shell. *Geophys. Astrophys. Fluid Dyn.* **89**, 23–43.

Franklin, J. 1972 Axisymmetric inertial oscillations of a rotating fluid. *J. Math. Anal. Appl.* **39**, 742–760.

Friedlander, S. 1982 Turning surface behaviour for internal waves subject to general gravitational fields. *Geophys. Astrophys. Fluid Dyn.* **21**, 189–200.

Friedlander, S. 1987 Internal waves in a rotating stratified spherical shell: asymptotic solutions. *Geophys. J. R. Astron. Soc.* **89**, 637–655.

Friedlander, S. & Siegmann, W. 1982*a* Internal waves in a contained rotating stratified fluid. *J. Fluid Mech.* **114**, 123–156.

Friedlander, S. & Siegmann, W. 1982*b* Internal waves in a rotating stratified fluid in an arbitrary gravitational field. *Geophys. Astrophys. Fluid Dyn.* **19**, 267–291.

Gans, R. 1983 Boundary layers on characteristic surfaces for time-dependent rotating flows. *J. Appl. Mech.* **50**, 251–254.

Greenspan, H. P. 1969 On the inviscid theory of rotating fluids. *Stud. Appl. Maths* **48**, 19–28.

John, F. 1941 The Dirichlet problem for a hyperbolic equation. *Am. J. Maths* **63**, 141–154.

Kumar, P. & Quateart, E. 1997 Angular momentum transport by gravity waves and its effect on the rotation of the solar interior. *Astrophys. J.* **475**, L143–L146.

Lister, J. & Buffett, B. 1995 How much of the Earth's core would be stably stratified if Nu < 1? *Phys. Earth Planet. Int.* **91**, 17–30.

Maas, L., Benielli, D., Sommeria, J. & Lam, F.-P. 1997 Observation of an internal wave attractor in a confined, stably stratified fluid. *Nature* **388**, 557–561.

Maas, L. & Lam, F. -P. 1995 Geometric focusing of internal waves. *J. Fluid Mech.* **300**, 1–41.

Phillips, O. M. 1963 Energy transfer in rotating fluids by reflection of inertial waves. *Phys. Fluids* **6**, 513–520.

Ralston, J. 1973 On stationary modes in inviscid rotating fluids. *J. Math. Anal. Appl.* **44**, 366–383.

Rieutord, M. 1987 Linear theory of rotating fluids using spherical harmonics. I. Steady flows. *Geophys. Astrophys. Fluid Dyn.* **39**, 163.

Rieutord, M. 1991 Linear theory of rotating fluids using spherical harmonics. II. Time periodic flows. *Geophys. Astrophys. Fluid Dyn.* **59**, 185–208.

Rieutord, M. 1995 Inertial modes in the liquid core of the Earth. *Phys. Earth Planet. Int.* **91**, 41–46.

Rieutord, M. 1999 A note on inertial modes in the core of the Earth. *Phys. Earth Planet. Int.* to appear, 1–12.

Rieutord, M. & Valdettaro, L. 1997 Inertial waves in a rotating spherical shell. *J. Fluid Mech.* **341**, 77–99 (referred to herein as paper I).

Saad, Y. 1992 *Numerical Methods for Large Eigenvalue Problems*. Manchester University Press.

Schaeffer, D. 1975 On the existence of discrete frequencies of oscillation in a rotating fluid. *Stud. Appl. Maths* **54**, 269–274.

Stewartson, K. & Rickard, J. 1969 Pathological oscillations of a rotating fluid. *J. Fluid Mech.* **35**, 759–773.

Stewartson, K. & Walton, I. 1976 On waves in a thin shell of stratified rotating fluid. *Proc. R. Soc. Lond.* A **349**, 141–156.

Unno, W., Osaki, Y., Ando, H. & Shibahashi, H. 1979 *Non Radial Oscillations of Stars*. University of Tokyo Press.

Wunsch, C. 1969 Progressive internal waves on slopes. *J. Fluid Mech.* **35**, 131–144.

Zahn, J.-P., Talon, S. & Matias, J. 1997 Angular momentum transport by internal waves in the solar interior. *Astron. Astrophys.* **322**, 320–328.

Zhang, K. 1995 Spherical shell rotating convection in the presence of a toroidal magnetic field. *Proc. R. Soc. Lond.* A **448**, 245–268.